RESEARCH PAPER

The Effect of the Isolator Size on the Efficiency of Rotary Piston Compressors

Savvas Savvakis*, Sotirios Damianos and Konstantinos Zoumpourlos

The SARM Project, Athens, Greece
*Corresponding author. E-mail: savvas@theSARMproject.com

Abstract

A hybrid renewable-hydrogen green energy system combines renewable energy sources with hydrogen production and storage technologies to create a sustainable and efficient energy system. One of the major components of such systems is compressors, which influence the system's overall efficiency. Therefore, this research paper will study design modifications that improve the efficiency of these components. More precisely, this study examines the correlation between a concentric rotary piston compressor isolator size and efficiency. The objective is to determine the significance of size on the compressor's performance. Two distinct mechanisms and operational designs employed in such compressors are investigated. Irrespective of the compressor design, it is revealed that the isolator's diameter considerably impacts the pressure ratio of these rotary compressors. Specifically, the conclusion is that a larger isolator increases efficiency; a 35% larger RSP diameter results in a 145% increase in peak pressure for Mechanism 1. A 100% larger RSP diameter yields a 180% boost in peak pressure for Mechanism 2.

Keywords: rotary, isolator, sliding port, efficiency, compressor, CFD, SARC, piston compressor, pressure ratio, compression ratio

1. Introduction

The transition to clean energy production through renewables is crucial in attaining the net-zero objective. Nonetheless, due to the inconsistent behaviour of renewable energy systems (RES), energy storage becomes vital to counteract this variability and unlock the full potential of renewable power sources. A plethora of storage alternatives are available; examples include flow batteries, which have limited deployment to date, sodium-sulfur batteries offering high energy density albeit with a disadvantageous hot liquid metal electrolyte reducing battery performance [1], supercapacitors which are incapable of supplying electricity for prolonged periods, as well as compressed air systems or flywheel options suitable only for small to medium-size applications due to location constraints [2]. Various criteria can be

used to categorize energy storage devices, such as capacity and storage period, lifespan, safety, environmental impact, cost and recyclability [3].

Hydrogen energy storage (HES) systems stand apart from other renewable energy storage systems owing to their versatility and ability to deliver multiple services [4]. This attribute is vital for grid operators to sustain system reliability and incorporate RES into infrastructures like electricity, heating, and transportation [4, 5]. HES systems facilitate large-scale energy storage, extending from 1 GWh to 1 TWh, whereas battery capacities usually range between 10 kWh and 10 MWh [5].

A compressor is an essential piece of equipment for HES designed to raise the pressure of gases or vapors by decreasing their volume. Various compressor types exist. Two common types are the positive displacement and dynamic compressors. Positive displacement compressors function by trapping the working medium followed by volume reduction, whereas dynamic compressors increase the pressure of the working medium by using its kinetic energy. Positive displacement compressors are distinguished from dynamic turbo-compressors with axial or radial flow configurations by their higher compression ratios and lower mass flow rates [6].

In many systems that depend on compressed fluids, compressors play a crucial role and are widely utilized for energy storage purposes. It is estimated that around 10% of global industrial electrical energy consumption is due to compressed gas [7] and rises to 20% if commercial and residential requirements like air conditioning systems, portable tools, pneumatic heating, ventilation, air pumps, etc. [8] are included. To cut down energy consumption, adopting energy-saving measures is crucial for the gas-compression industry which faces an increasing global demand. Recent strategies implemented upstream and downstream improvements of gas compressors, by reducing pipeline leakages, minimizing frictional losses, and enhancing the efficiency of end-use devices within the compressed gas systems. However, existing compressor technologies can only achieve estimated future savings of up to 15% (740 TWh in 2012), given the maximum power and power-to-weight ratios [9].

The ability to generate maximum pressure during the compression process (minimum volume) remains a significant concern in compressor technology. Consequently, continuous research and development efforts are directed towards design optimization across all compressor types. Recently, a market analysis study revealed that rotary compressors dominate the global compressor market and are projected to retain this position until 2028 (Grand View Research, 2021) [10] and substantial research is being directed toward improving rotary compressor performance. It is noteworthy that in some instances, as with the present study, design optimization can yield considerable efficiency enhancements. For example, Ooi conducted a theoretical investigation and forecasted a 50% decrease in

mechanical loss, resulting in a greater than 14% improvement in the rolling piston compressor's performance coefficient [11]. Liu *et al.* employed the gradient-search technique to optimize scroll compressor bearing components and observed a minimum of 14.1% reduction in frictional losses at these components [12]. Etemad and Nieter pinpointed the starting angle and wrap height as critical geometric parameters of scroll compressors but provided no numerical data; their work merely identified parameters with the greatest impact on overall efficiency [13]. According to Hirayama *et al.*, enhancing a rotary vane compressor utilized in refrigeration systems with an extra cylinder and an additional bearing on the main shaft can improve reliability, capacity, performance by as much as 9% [14]. Meng *et al.* proposed an innovative rolling piston rotary compressor cylinder design that elevated electric efficiency by 4.43% [15]. Savvakis *et al.* managed to lower the secondary peak pressure of rotary piston compressors by 130% and increasing the efficiency to nearly 14% [16]. Noh *et al.* examined how cylinder slenderness ratio affects rolling piston compressor performance and discovered that reducing this ratio increased volumetric efficiency by 6.3%, culminating in a total efficiency improvement of 3.7% [17]. Gu *et al.* scrutinized vane tip gap height sensitivity and deduced that as the gap broadens (0.01–0.05 mm), isentropic efficiency declines by 18.26% [18].

The described piston rotary technology falls under the positive displacement compressor category. This concept is based on a concentric rotary technology that has existed for 40 years and is utilized in internal combustion engines, pumps, expanders, and compressors. The construction of this particular concentric rotary device comprises four primary components: two rotors, a piston, and a housing. One rotor (2) (known as the piston rotor) is connected to the piston (1), while the other rotor (3) (referred to as the isolator rotor) features a cavity (4) that accommodates the piston (1) when it aligns with the isolator rotor's (3) outer edge (Figure 1). The isolator rotor's (3) function is to confine the working fluid ahead of the piston (1), generating a compression chamber (depicted in orange in Figure 1) between the piston, the isolator rotor's periphery, and the housing.

The concentric rotary piston technology addressed herein falls under the positive displacement compressor category. This concept has been in existence for 40 years and is employed in internal combustion engines, pumps, expanders, and compressors.

The concentric rotary technology concept design under examination primarily consists of two rotary discs, or rotors. The first rotor, denoted as the piston-disc (2), has a fixed piston (1) positioned along its periphery, which serves to compress the working fluid. Attached to a shaft, the piston (1) follows a circular orbit. The second rotor functions as a rotary sliding port (RSP) or isolator (3), capturing the working fluid in front of the piston (1) and compressing it during the piston's rotational
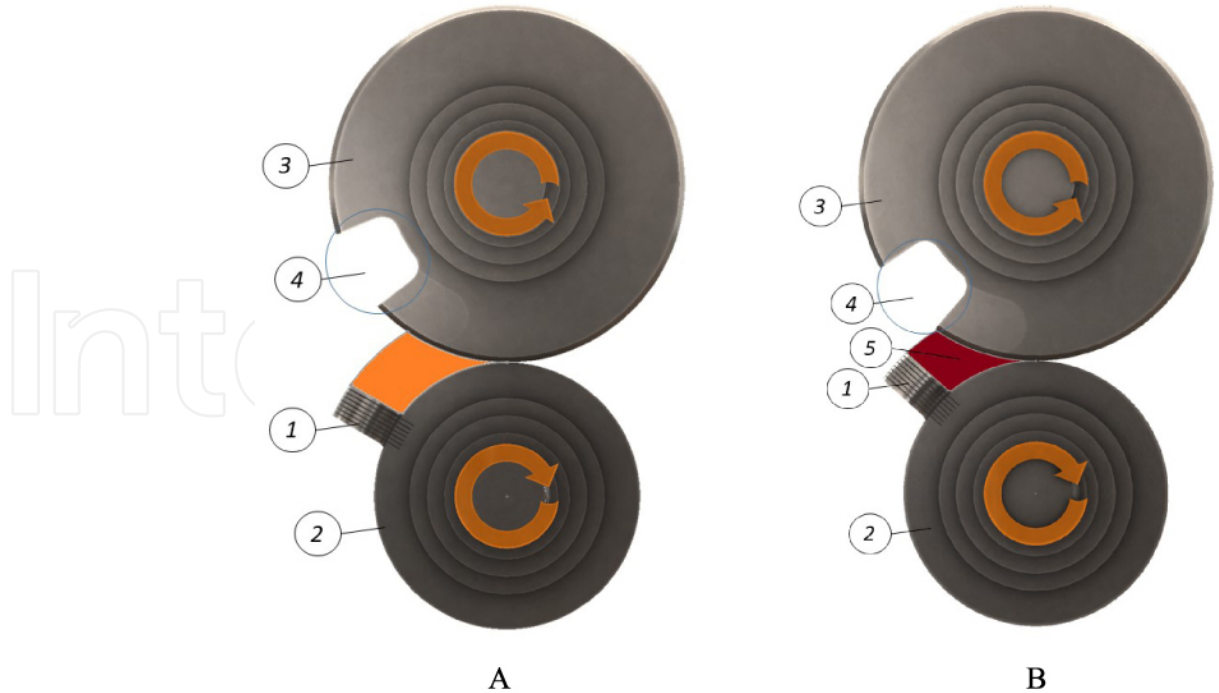
Figure 1. Description of the operating principle of the SARC compressor (SAvvakis Rotary Compressor).

movement (Figure 1A). To prevent collisions between the piston and RSP during operation, a carefully designed cavity (4) encapsulates the piston within the RSP.

Figure 1(B) illustrates the completion of the compression process as the pressure within the compression chamber (5) reaches its maximum value (peak pressure). Subsequently, exposure of the cavity to the compression chamber leads to the expansion of the working fluid and a decrease in pressure. A full compression cycle concludes when exposure of the intake chamber to the compression chamber ceases, and the compression process resumes.

The four concept designs based on this operating principle are the following. In 1980, Emmanouil Andreas Pelekis originated and patented this approach by developing a compression mechanism utilizing concentric circular motion of vanes within a segmented annular region [19]. His patent dealt with a compression mechanism that achieves compression by a circular concentric motion of a vane (A & B) inside a segmented annular region. In Figure 2, the region enclosed by points A, B, C, and D denotes the compression chamber.

In 2005, Ronnie Duncan patented a concentric rotary internal combustion engine with an aim towards downsizing Pelekis' technology by integrating a smaller isolator rotor into the piston-rotor space [20] (Figure 2).
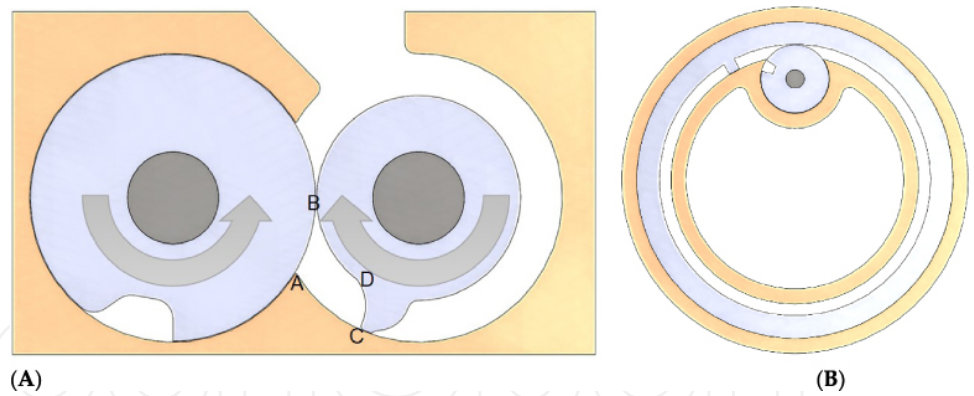
Figure 2. (A) Section view of the Emmanouil Andreas Pelekis apparatus (EP0046586A2) [19]; (B) Section view of the Duncan engine (US20050284440A1) [20].
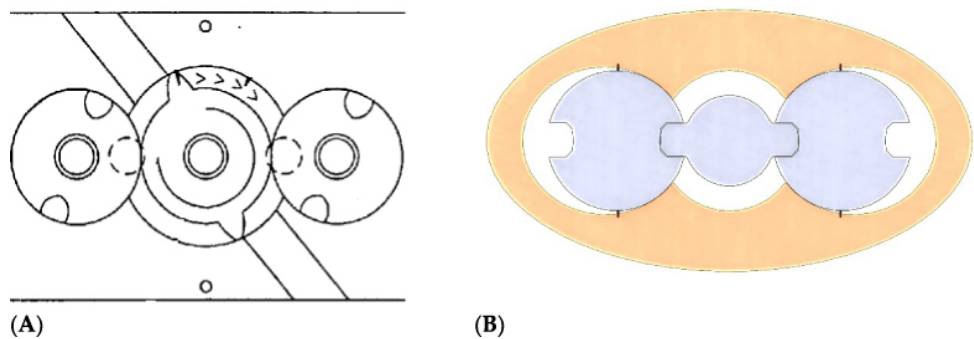
Figure 3. (A) Jerome Lurtz's rotary technology (US20060120910A1) [21]; (B) an apparatus by ASTRON AEROSPACE LLC (WO2021029906A1) [22].

The third rotary technology was patented in 2006 by Lurtz [21], featuring a mechanism with three rotors engaged in concentric synchronized motion. The central rotor possesses two pistons at a 180° angle from each other, while the side rotors each contain two cavities (Figure 3).

Recently, ASTRON AEROSPACE LLC unveiled a technology in 2021 bearing similarities to Jerome Lurtz's rotary mechanism, as depicted in Figure 3 [22]. The primary distinction between these patents lies in their respective insulation methods.

In all these discussed designs, a crucial factor that remains unaddressed by inventors pertains to the size of the isolator rotor. This rotor connects to two distinct shafts, which are concurrently linked through a gear pair. As the piston operates, it compresses the working fluid until reaching its primary peak pressure (denoted in Figure 1 by label 5), which subsequently becomes the output pressure of the

compressor following the completion of the compression process. Nevertheless, the isolator's size is critically important for achieving optimal performance in these compressors.

Generally, the compression ratio (CR) is an integral parameter associated with the performance of all types of compressors. For rotary piston compressors, CR heavily relies on the duration of interaction between piston and RSP. A longer interaction time results in a reduced amount of air that can be trapped and compressed by the piston. Consequently, this study aims to minimize this interaction time.

The SARC compressor, illustrated in Figure 1, exhibits several advantages compared to other compressor types. First, it generates enhanced isentropic efficiency (>90%). The absence of contact between moving components or stationary parts enables oil-free operation. Moreover, the avoidance of rotating components to contact stationary machine elements restricts mechanical losses to bearing components only and the frictionless movement of rotating elements along with oil-free assembly contributes to lower construction and maintenance expenses. Notably, this concentric rotary technology can attain greater speeds than reciprocating and eccentric rotary compressors as it does not encounter any direction-altering inertial forces during operation. Consequently, minimal inertial forces induce no stress-related issues at elevated speeds. Furthermore, these benefits are accompanied by a simple, lightweight design leading to reduced construction costs and increased profitability across various operations.

2. *Proposed solution*

This research demonstrates that the CR increases as the RSP diameter increases (Figure 4). When enlarging the RSP diameter, despite maintaining a constant position angle φ' (Figure 4), the interaction angle φ becomes shorter (Figure 5). The interaction angle signifies the angle at which the piston engages with the RSP. During this period (interaction time), communication takes place between the compression and intake chambers; subsequently, the compression process resumes when the RSP separates these chambers. A reduced interaction time diminishes the piston's transit duration through the RSP, resulting in earlier isolation of the compression chamber from the intake chamber, and prolongation of the compression process, ultimately leading to a higher CR.

It is important to note that while temperature does increase, it does so to a lesser extent compared to pressure. Nevertheless, consideration of thermal expansion due to elevated temperatures is crucial. Furthermore, heat management should address higher temperatures arising from an increased CR, and accommodating larger diameters must take into account greater dynamic loads and spatial constraints. To summarize, identifying an optimal diameter constitutes an optimization problem involving all previously mentioned parameters.

Figure 4. SARC with the nominal (left side) and double RSP diameter (right side).
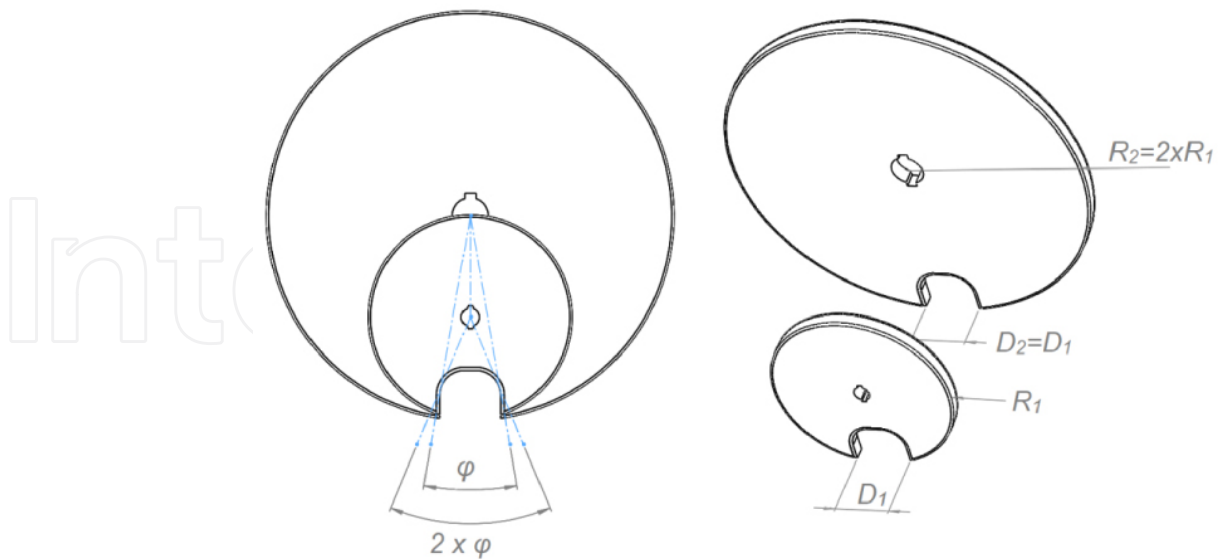
Figure 5. Interaction angle φ for two different RSP sizes.

As depicted in Figure 4, a higher CR also results from a larger RSP reducing the size of compression chamber (6). A portion of this chamber is occupied by the RSP

(depicted by region 7 in the same figure). However, the shorter interaction time between piston and RSP is the main reason for the higher CR rather than the smaller compression chamber (6) caused by the region 7.

3. Methodology

Initially, a watertight 3D fluid model was developed using the pre-processor ANSA [23]. Following the definition of property IDs and boundary conditions, the file was exported in STL format for utilization in the CFD solver CONVERGE [24]. Boundaries are the rotating and stationary walls with a constant temperature & absolute roughness zero and the pressure-inlet boundary that indicates the intake port (Figure 6). The model employs a Navier–Stokes density-based solver with a 1.01 bar pressure inlet and a 300 K temperature inlet. The choice of CONVERGE was based to its unique capability of automatically constructing polyhedral meshing, significantly reducing pre-processing time and simplifying case-setup modeling. Lastly, output data analysis was conducted with the post-processor META, which facilitated model visualization and animation. The geometry and results files were incorporated into the software, and final conclusions were determined after analyzing each state.

Figure 6. Intake port position and dimensions.

The operating speed of the machine was designated to 4000 rpm, with a base grid size of 0.02 m in each Cartesian direction (X, Y, Z). In comparison to asymmetrically structured compressors like variable displacement vane pumps [25],

the concentric configuration of this compressor permits high-speed operation. Notwithstanding, rotary vane compressors [14] surpass 4000 rpm, while screw compressors reach beyond 6000 rpm [26]. The maximum achievable speed for the current compressor is not limited to 4000 rpm; its weight-balanced design enables even higher speeds (pending patent application prior to publication). In theory, it operates at an equivalent rotational speed to a gas turbine (e.g., 30,000 rpm). However, based on CFD simulations, the peak pressure ratio (22.8) is attained at 4000 rpm and optimal efficiency at 6400 rpm for the present design. High speed is crucial for maintaining sealing efficacy and promoting heavy-duty industrial usage with elevated flow rates. Consequently, SARC is a smaller and lighter machine in comparison to other commercial compressors due to high flow rates and high speeds. Conversely, flow rates are directly proportional to speed—requiring machinery adjustments such as smaller piston orbit or diameter for low flow rate applications while maintaining high-speed performance. Regarding boundary conditions, smooth walls were assumed and a symmetry plane was employed to expedite convergence. Neither of these factors adversely affect result accuracy because the focus lies on a qualitative comparison of RSP sizes rather than achieving a more realistic simulation outcome. Furthermore, a sealing feature was implemented with the symmetry plane to ensure compressed air remains within the domain.

Table 1 demonstrates grid-independent calculations using three mesh refinements in order to enhance computational precision and efficiency. 0.8 M cell grids were doubled across sequential refinement stages (0.8 M, 1.6 M, 3.2 M). The mesh's density significantly impacts simulation results. Using the Richardson extrapolation method [27], the Grid Convergence Index (GCI) for peak pressure rates was calculated for each mesh variant, and ultimately settled upon a 2.4 M cell grid for final simulations.

Table 1. Discretization error calculations based on the Richardson extrapolation method.

	Φ = **Pressure (Pa)**
N1 ($\times 10^6$)	3.2
N2 ($\times 10^6$)	1.6
N3 ($\times 10^6$)	0.8
GCI21	0.145%
GCI23	0.85%

As high-velocity gradients are present near walls [28], grid refinement is necessary for accurate boundary-layer flow representation. Average $y+$ values were calculated to meet boundary-layer mesh requirements for the RNG (Re-Normalisation Group) k-epsilon Reynolds-averaged Navier–Stokes (RANS) turbulence model—typically ranging from 30 to 300—with labyrinth walls set to 85, piston side walls at 175, and

chamber walls at 50. In instances of extremely low $y+$ values, the proximity of the wall region experiences a substantial impact from viscous effects, rendering the wall functions in the RNG k-epsilon model potentially ineffective. Conversely, with elevated $y+$ values, the turbulence model might inadequately represent near-wall flow physics, leading to imprecise predictions of flow behaviors. As such, for a precise and dependable turbulent flow simulation the $y+$ values should be within an acceptable range.

The fluid flow is governed by the Redlich–Kwong equation for compressible gas and air which offers greater accuracy than Van der Waals or ideal gas equations. The wall properties are considered to be smooth, having an absolute roughness set to 0. As for turbulence modelling, the RNG $k–\varepsilon$ RANS model was chosen due to its ability to enhance accuracy in rotating flow scenarios [29]. The scheme for the solution method is transient, with the convergence criterion based on the PISO algorithm alongside a tolerance value of 10^{-3}.

Upon defining a grid-independent mesh, the subsequent convergence criterion stipulated that maximum pressure and temperature variations between subsequent cycle calculations must not exceed 3%. To achieve a constant primary peak pressure value, each case required simulation over five or six cycles.

The compression chamber lacks a discharge port; instead utilizing a blind configuration because discharge port location, size and timing significantly influence rotary compressor performance. After the compression process' completion, the pistons enters into the cavity of the rotating isolator and both chambers (intake and compression) communicated with each other. At that moment, any small amount of compressed air trapped between the piston and the isolator's cavity expands into the low pressure area, similar to the gas trapped in the dead space in reciprocating compressors. For more information about this mechanism and the reason of a high pressure development right after the communication of the intake chamber with the compression chamber, reader is referred to the paper "The Effect of the Isolator Design on the Efficiency of Rotary Piston Compressors" [16]. This method establishes a proof of concept for the compressor's sealing approach while minimizing uncertainties. The primary objective involves attaining maximum pressure without environmental leakage and minimal leakage around the piston's toroidal wall.

According to a previous optimization study (pending paper approval), which determined the intake port's position and size, the optimal intake port (7) is tangential to the intake chamber's outer periphery and proximate to the isolator periphery. The design should be circular and of minimal dimensions, considering the specific compressor size. In this instance, the diameter measures 12.5 mm (see Figure 5).

This research encompasses both designs of rotary machines that could serve as rotary piston compressors, investigating the impact of the RSP size for each design.

(A) − mechanism 1

(B) − mechanism 2
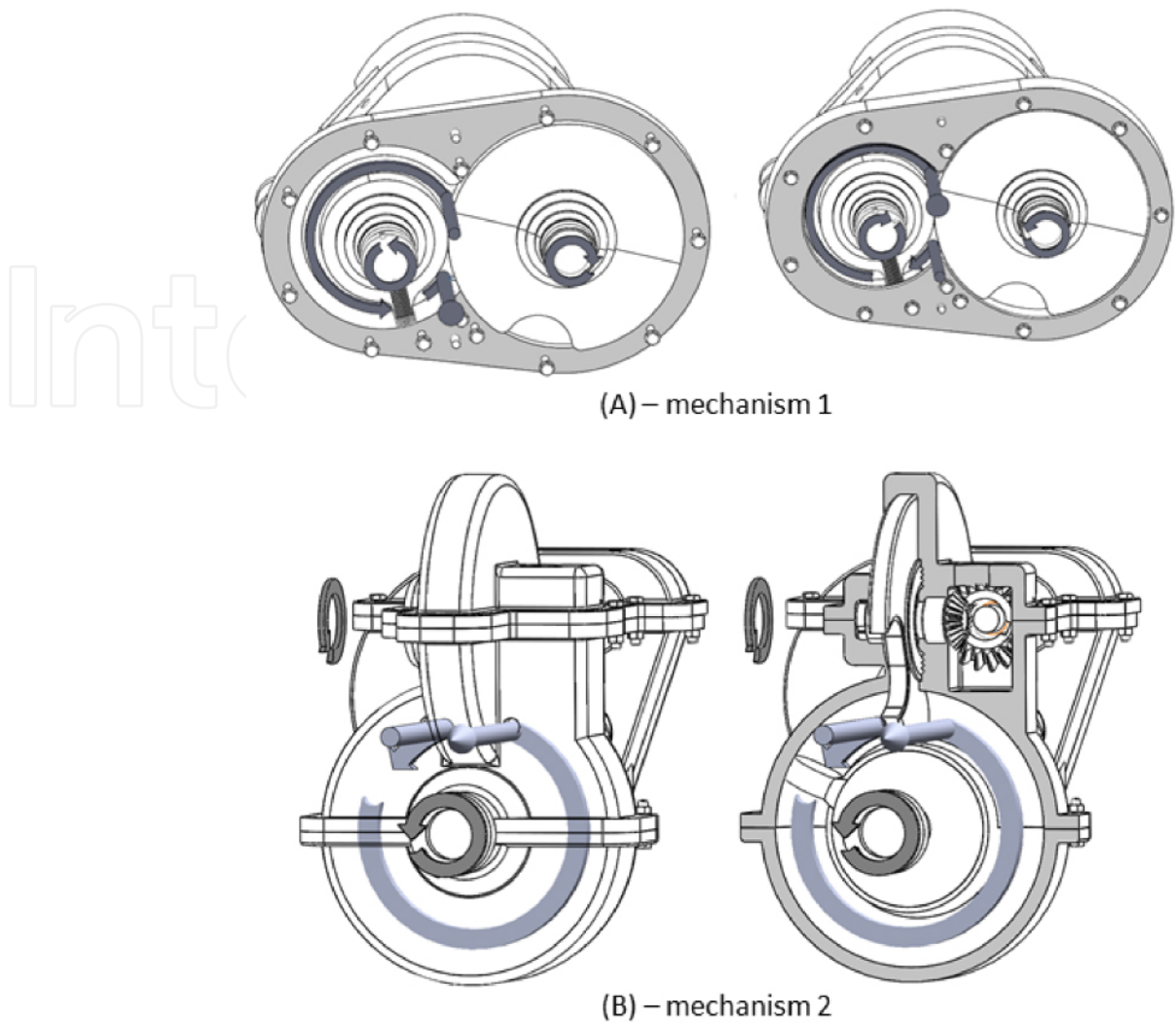
Figure 7. A comparison of the two alternate designs based on the same operational principle.

Figure 7 exhibits the two distinct designs, with the sole distinction being the orientation of the plane on which the RSP revolves. In the top design (mechanism 1), the piston's circular motion occurs on a plane parallel to that on which the RSP rotates. Conversely, in the bottom design (mechanism 2), the piston's circular trajectory lies on a plane perpendicular to that where the RSP revolves.

4. Experimental procedure and verification

A prototype utilizing mechanism 1 was developed using Aluminum 7075-T6 to validate results, as depicted in Figure 8. The experiments were conducted at Aristotle University of Thessaloniki's Laboratory of Applied Thermodynamics, an affiliated member of EARPA (European Automotive Research Partners Association).
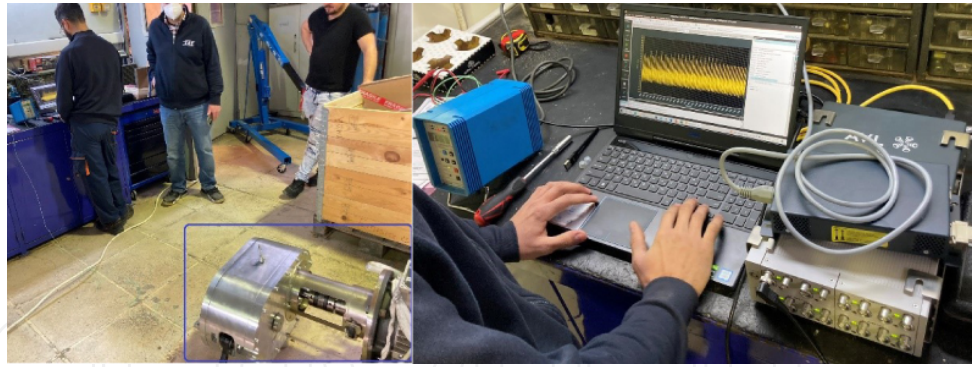
Figure 8. Completed rotary piston compressor assembly and images from the experimental process.

The laboratory is also QMS-certified and adheres to ISO 9001:2008 requirements. Pressure measurements were obtained using the AVL X-Ion high-speed, modular data acquisition system and power analyzer. Capable of capturing signals at exceptionally high-frequency sampling rates (>100 kHz), the AVL X-Ion connects to Kistler 5011 signal amplifier tied to an in-cylinder pressure sensor. During experimentation, a variable frequency motor maintained a consistent speed of 2576 rpm while driving the compressor. Outlet pressure readings were obtained from an outlet pressure sensor situated where peak pressure development was theorized. Notably, measured peak pressure at 2576 rpm closely aligned with CFD outcomes. Attributed to the first five rotations, CFD simulations indicated a peak pressure of 20.477 bar, while measurements during testing exceeded 1000 rotations. As illustrated in Figure 9, peak pressure values oscillated between 15.53 and 21.29 bar. The horizontal axis in the graph represents time in milliseconds (msec), while the vertical axis indicates pressure in bar.

5. *Results*

5.1. Mechanism 1

In order to expedite the simulation process, the RSP size for the first mechanism is not made twice as large as the nominal size. The standard RSP diameter stands at 212.3 mm, while the augmented RSP exhibits a diameter of 270.30 mm. As evidence of valid results, Figures 10 and 11 depict the convergence diagrams for both the small and large RSP sizes. These figures demonstrate that four cycles are required for each simulation to achieve a divergence of less than 3%. Furthermore, temperature converges more rapidly than pressure in both instances.

Subsequently, the simulations were conducted with varying time-step sizes until a time-step independent simulation was attained. A comparison of pressure
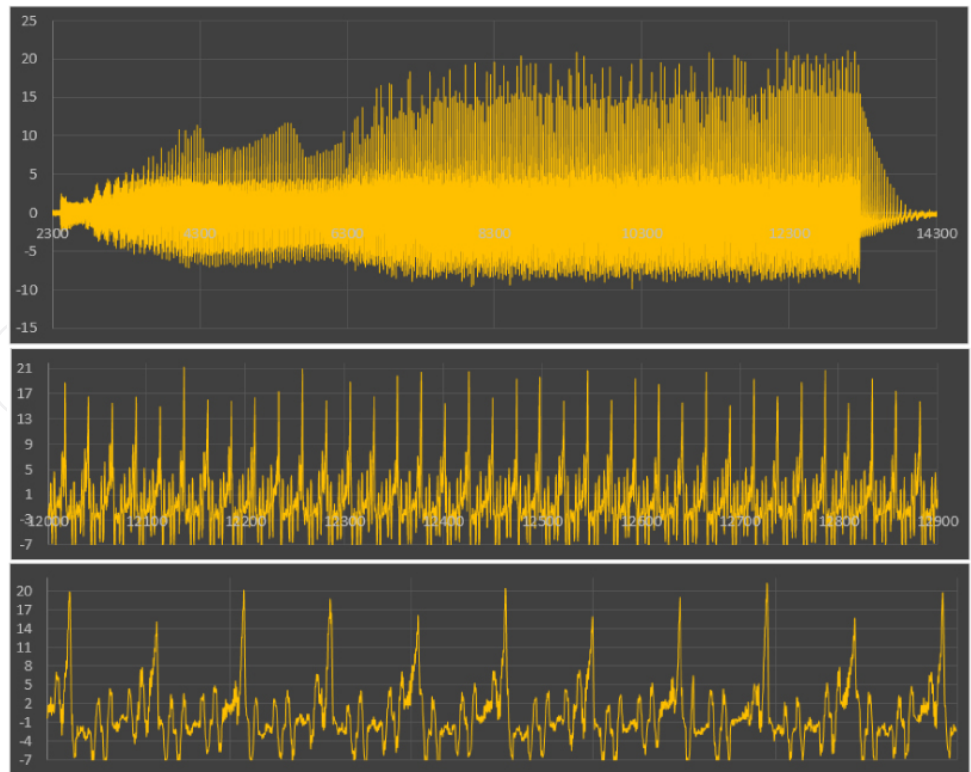
Figure 9. Recorded test outcomes at 2756 rpm.
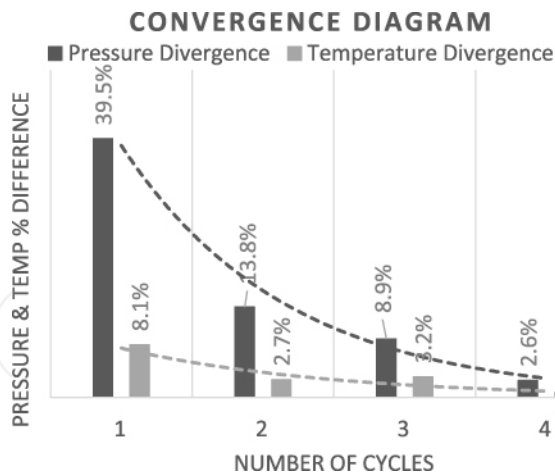
Figure 10. Convergence diagram for the nominal RSP diameter.

development across both RSP sizes can be observed in Figure 12. A 27.35% increase in RSP diameter causes the peak pressure to occur 10° later, resulting in an elevated CR and peak pressure value. Peak values for each RSP size are presented in Table 2.

Figure 13 illustrates the effect of RSP diameter on temperature, indicating that an enlarged RSP causes the maximum temperature to appear 10° later; however, it does

CONVERGENCE DIAGRAM

■ Pressure Divergence ■ Temperature Divergence
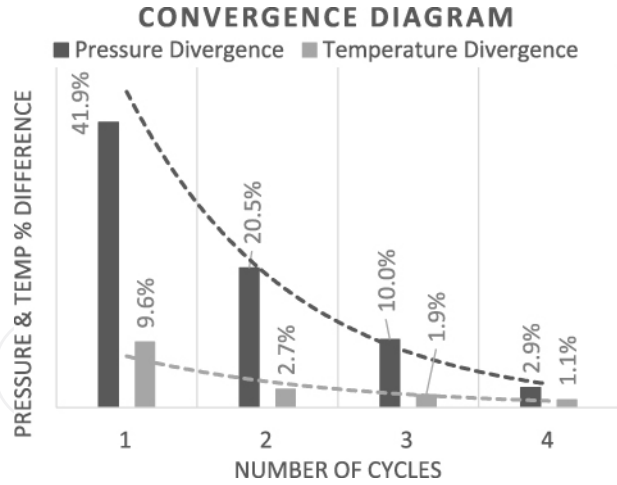
Figure 11. Convergence diagram for the larger RSP diameter.

Pressure

—— extented RSP   ----· nominla SP
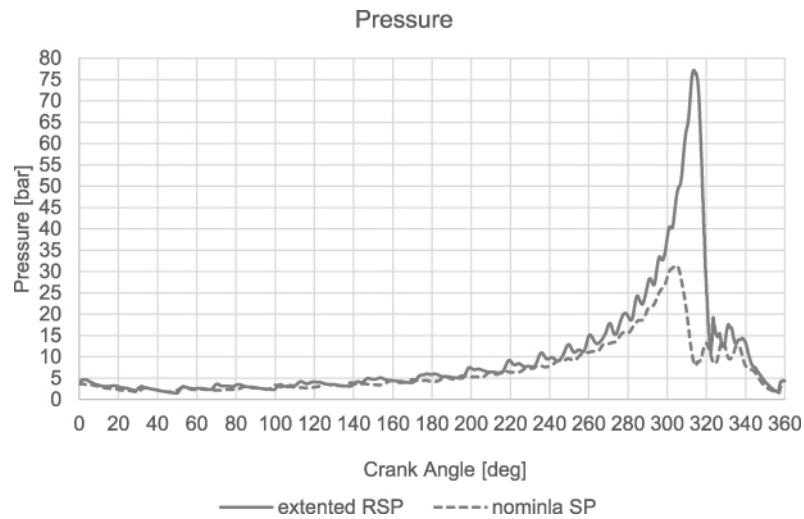
Figure 12. Pressure development during one operating cycle for Mechanism 1 for two different RSP diameters.

Table 2. Main variables for Mechanism 1.

Sliding port diameter D (mm)	Peak pressure (bar)	Peak temperature (K)	Peak density (kg/m^3)
R = 106.15 mm	31.41	740.62	14.62
R = 135.15 mm	77.02	934.49	28.154
Deviation (%)	145.2%	26.18%	92.57%

not increase as significantly as pressure. This increase in temperature may contribute to thermal and structural challenges for both the piston and isolator
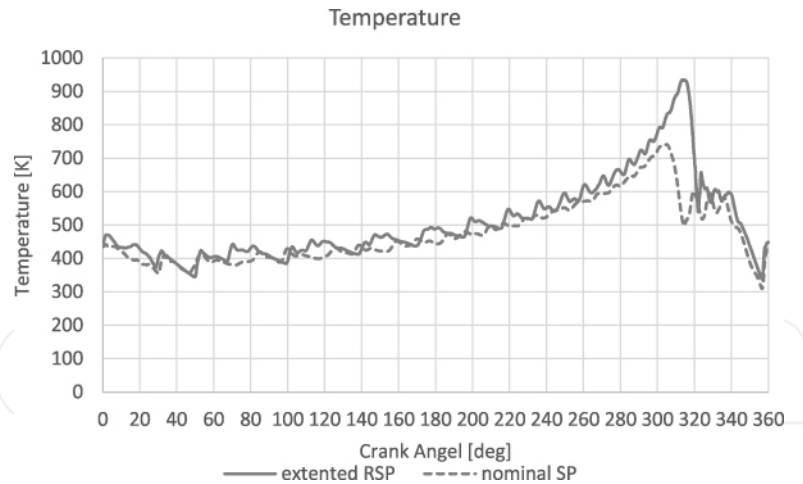
Figure 13. Temperature development for mechanism 1 for the two different RSP diameters.
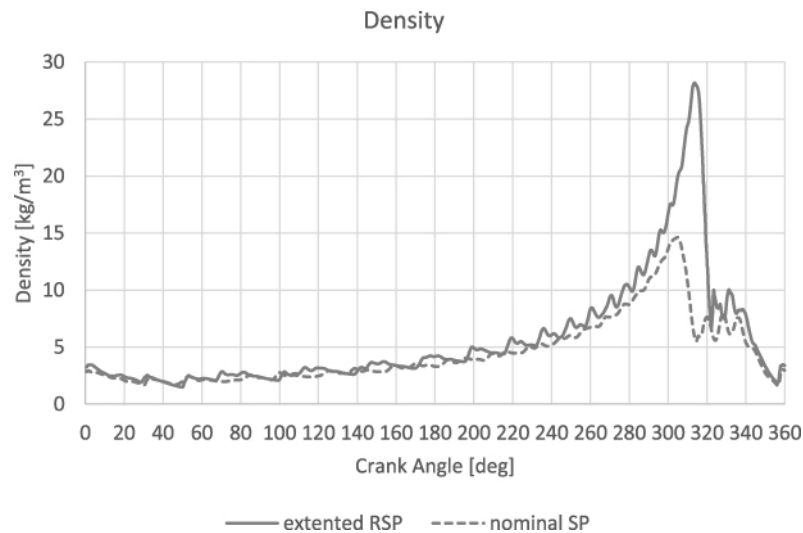
Figure 14. Density for every crank angle for mechanism 1.

(RSP), necessitating alternative materials or a modified cooling management strategy due to the higher CR.

Similarly, Figure 14 reveals that density follows a pattern comparable to pressure. The maximum value is considerably higher with a larger RSP diameter, and the two curves closely resemble each other, except for the area surrounding the compression process' completion where the pressure/density rises substantially more rapidly.

Figures 15 and 16 display pressure and temperature contours at the end of the compression process for both RSP sizes. Notably, when employing a larger RSP, the piston is situated 10° closer to the RSP periphery at the end of the compression process. In the case of an increased RSP, the cavity within the RSP accommodating the piston as it moves through the periphery possesses a greater linear velocity.
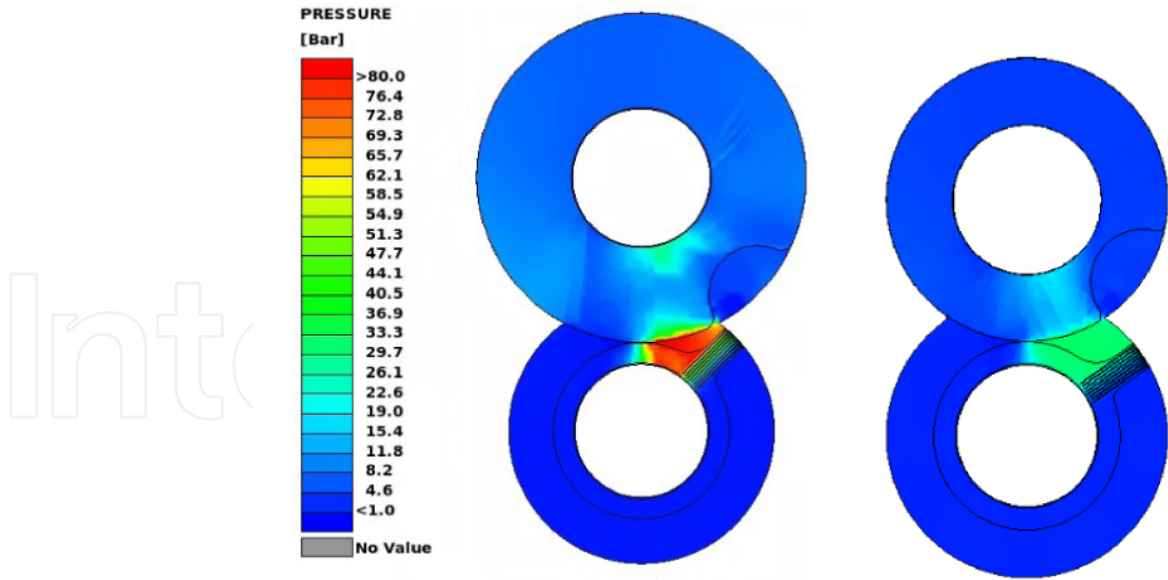
Figure 15. Comparison of the pressure at the end of the compression process.
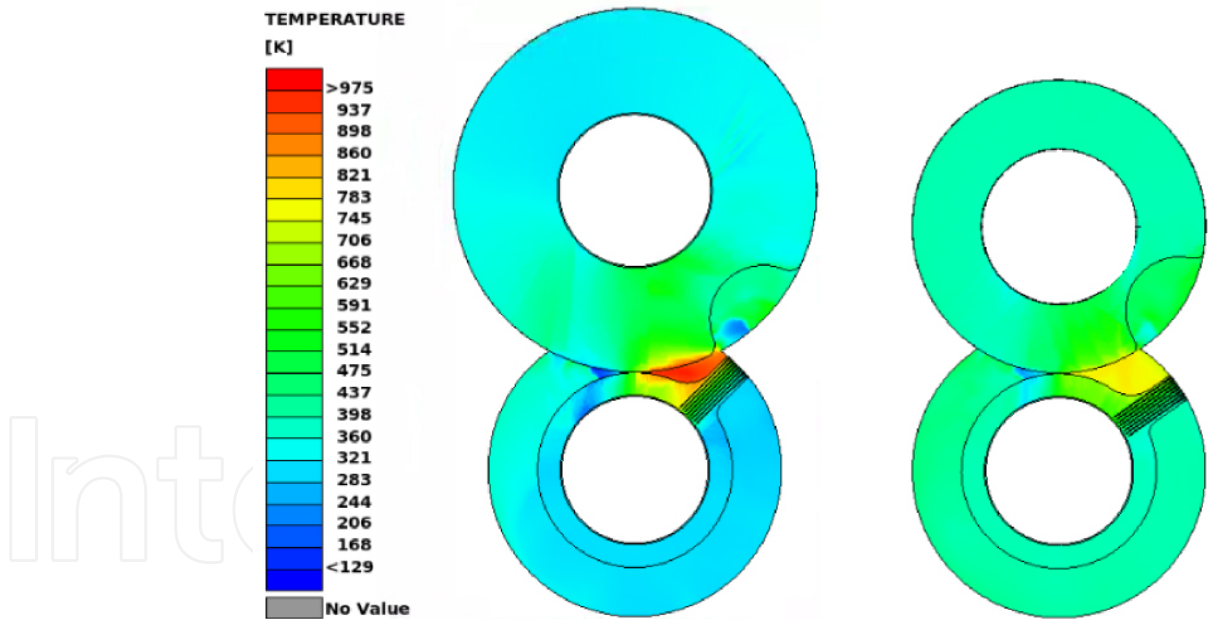
Figure 16. Comparison of the temperature at the end of the compression process.

Consequently, it requires a smaller arc to encompass and facilitate the piston. This shorter interaction arc primarily accounts for the elevated CR and peak pressure observed with a larger RSP (Figure 16).

Interestingly, despite having a higher peak temperature, lower temperatures develop along the side areas of an enlarged RSP.

Figure 17. Mechanism 2 with nominal RSP diameter.
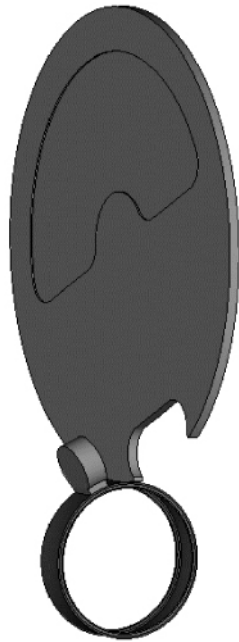
Figure 18. Mechanism 2 with double RSP diameter.

5.2. Mechanism 2

Figures 17 and 18 present the rotating components of the second Mechanism CFD model, wherein the larger RSP is twice the size of its nominal counterpart. Convergence diagrams for this mechanism are depicted in Figures 19 and 20, which display analogous behavior to Mechanism 1 by converging after four cycles. The temperature exhibits a quicker convergence than pressure; however, an additional cycle is required to achieve a divergence goal below 3%.

The progression of pressure, temperature, and density is illustrated in Figures 21, 22 and 23, respectively.
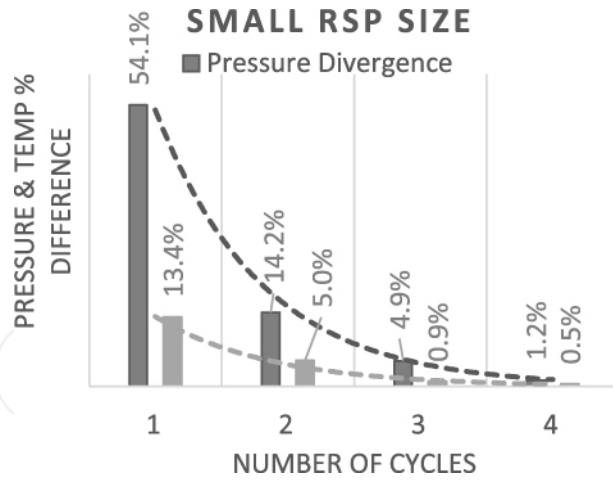
Figure 19. Convergence diagrams for nominal RSP diameter.
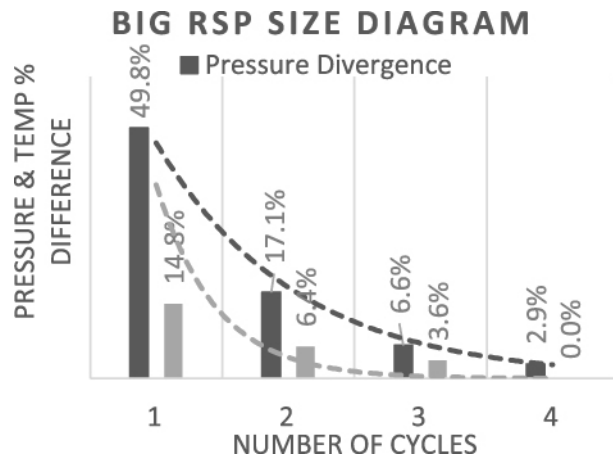
Figure 20. Convergence diagrams for double RSP diameter.
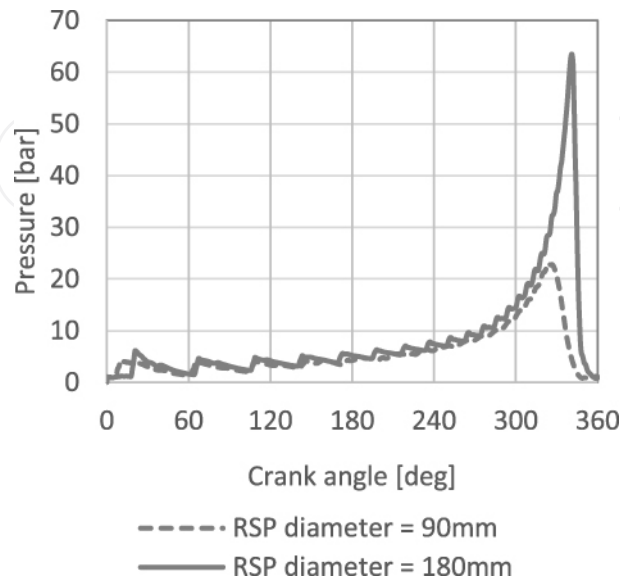
Figure 21. Pressure for every crank angle for mechanism 2.
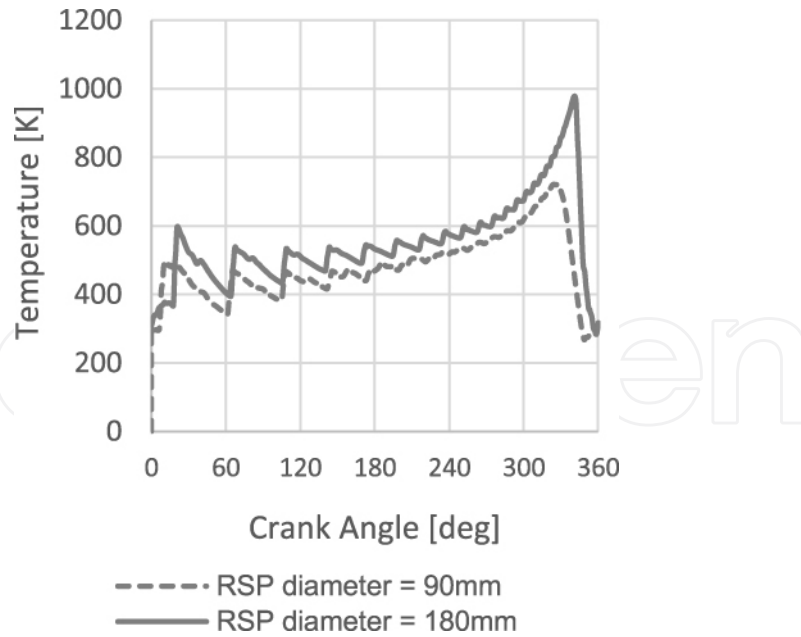
Figure 22. Temperature for every crank angle for mechanism 2.
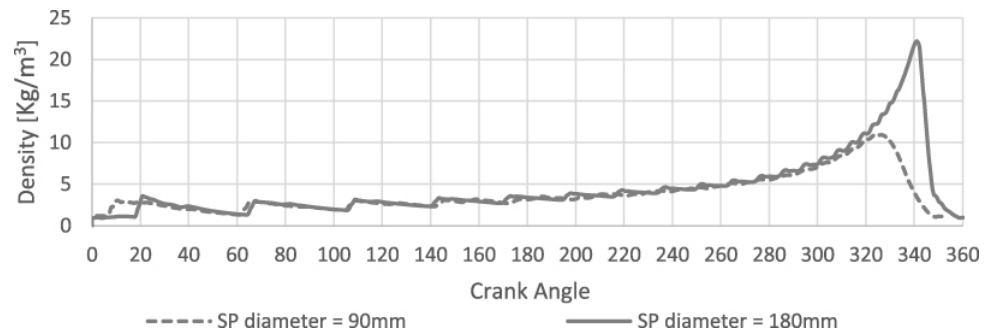
Figure 23. Density for every crank angle for mechanism 2.

Table 3 presents the peak values of pressure, temperature, and density for both RSP sizes. It should be noted that Mechanism 2 does not exhibit the same pressure increase as Mechanism 1. Specifically, a 35% increase in the RSP diameter for Mechanism 1 resulted in a 145% surge in peak pressure, while doubling the RSP diameter (100%) for Mechanism 2 led to a mere 180% boost in peak pressure. This implies that Mechanism 1 is more susceptible to RSP size variations compared to Mechanism 2.

Upon doubling the sliding port diameter in Mechanism 2, peak values emerge 15° later. Figures 24 and 25 compare the pressure developed at the end of the compression process, while Figures 26 and 27 compare respectively the temperature

Table 3. Main variables for mechanism 2.

Sliding port diameter D (mm)	Peak pressure (bar)	Peak temperature (K)	Peak density (kg/m^3)
D = 90 mm	22.946	721.406	10.969
D = 180 mm	63.491	978.704	22.179
Deviation (%)	180.27%	35.67%	102.2%
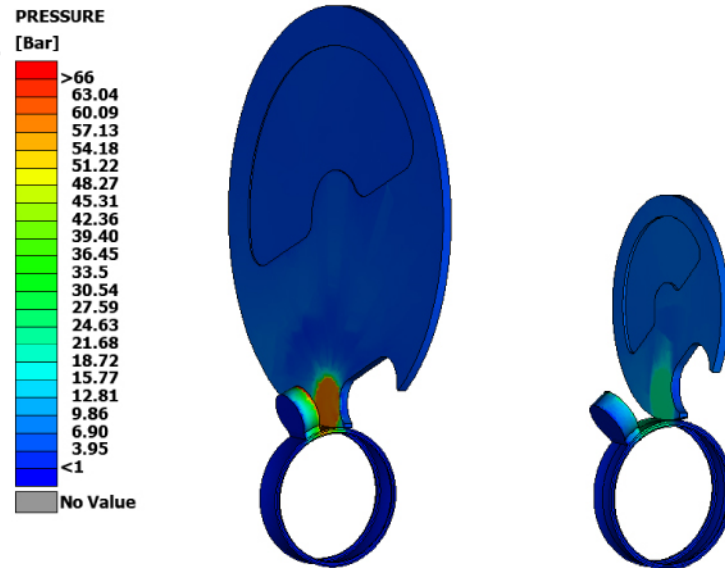
Figure 24. Pressure distribution comparison.
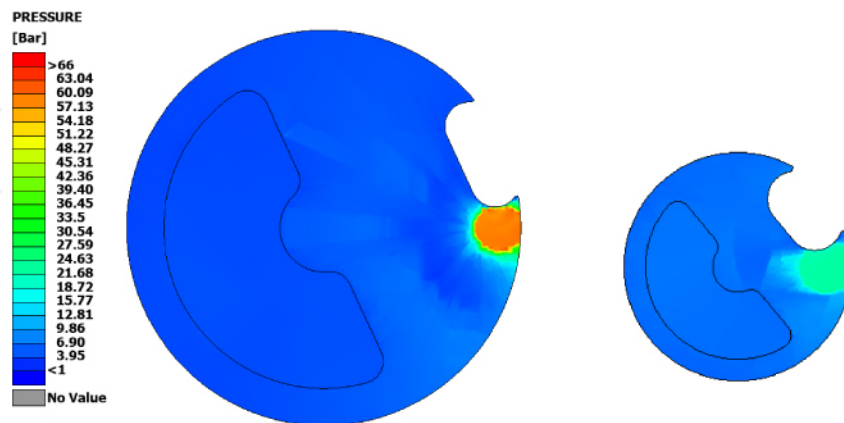
Figure 25. Pressure distribution comparison for RSP.

at that moment. The values are obviously higher for the bigger RSP, since the CR in the case of a bigger RSP is higher.

Figure 26. Temperature distribution for both RSP sizes.
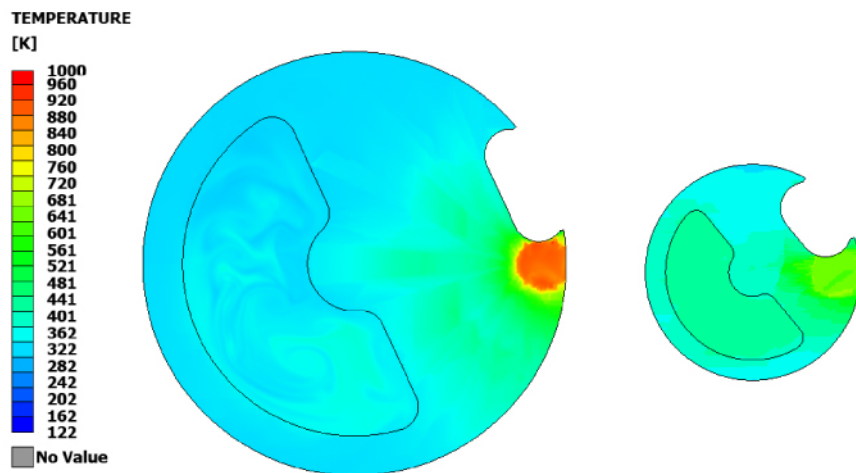
Figure 27. Temperature distribution for RSP.

6. Conclusion

Amplifying the rotary sliding port (isolator) diameter enhances the compression ratio and pressure output of rotary piston compressors without altering any other critical components, irrespective of the compressor's mechanism. However, Mechanism 1 attains a superior compression ratio compared to Mechanism 2 due to its involvement with the RSP periphery as part of the compression chamber. Consequently, increasing the RSP diameter reduces the end volume of the compression chamber (as depicted in Figure 7), leading to a further escalation in peak-pressure value relative to Mechanism 2.

The greater peak pressure observed in Mechanism 2 is caused only by the reduced interaction time between piston and RSP. In Mechanism 2, an RSP sidewall constitutes part of the compression chamber; thus, alterations in RSP periphery size do not affect the end volume of said chamber. The different components employed for defining compression chambers in both mechanisms explain why a 35% increase in RSP diameter results in a heightened peak pressure of 145% for Mechanism 1 and a substantially larger RSP diameter of 100% yields a 180% increased peak pressure for Mechanism 2.

Abbreviations

CFD	Computational Fluid Dynamics
CR	Compression Ratio
GCI	Grid Convergence Index
HES	Hydrogen Energy Storage
RES	Renewable Energy Sources
RSP	Rotating Sliding Port
SARC	SAvvakis Rotary Compressor

Conflict of interest

The authors declare no conflict of interest.

Acknowledgements

References

1 Chen H, Xu Y, Liu C, Fengjuan H, Hu S. 32 – storing energy in China—an overview. In: *Storing energy*. 2nd ed. Amsterdam: Elsevier; 2022. p. 771–791.

2 Mahmoud Morsi Ali D. Hydrogen energy storage. In: *Energy storage devices*. InTechOpen: London; 2019.

3   López González E, Isorna Llerena F, Silva Pérez M, Iglesias FR, Guerra Macho J. Energy evaluation of a solar hydrogen storage facility: comparison with other electrical energy storage technologies. *Int J Hydrogen Energy*. 2015;**40**(15):5518–5525.

4   Widera B. Renewable hydrogen implementations for combined energy storage, transportation and stationary applications. *Therm Sci Eng Prog*. 2020;**16**: 100460.

5   Melaina M, Eichman J. *Hydrogen Energy Storage: Grid and Transportation Services (Technical Report)*. Golden, CO: NREL; 2015. p. 1–66.

6   Bloch HP. *A practical guide to compressor technology*. Hoboken, NJ: Wiley; 2006.

7   Radgen P. *Compressed air systems in the Europian Union: energy, emisions, savings potential and policy actions*. Ludwigsburg: LOG_X Verlag GmbH; 2001.

8   US Department of Energy and Energy Efficiency and Renewable Energy. *Improving compressed air system performance: a sourcebook for industry*, US, 2003. Available from: https://zagroscompressor.com/wp-content/uploads/2019/11/Improving_Compressed_Air_System_Performance_A_Sourcebook_for_Industry.pdf.

9   Cipollone R, Vittorini D. Energy saving portential in existing compressors. In: *Proceedings of the 22nd International Compressor Engineering Conference*. Purdue, IN: Purdue University; 2014.

10 Grand View Research. *Air compressor market size analysis report, 2021–2028 [Internet]*; 2021. Available from: https://www.grandviewresearch.com/industry-analysis/air-compressor-market.

11 Ooi KT. Design optimization of a rolling piston compressor for refrigerators. *Appl Therm Eng*. 2005;**25**(5–6):813–829.

12 Liu Y, Huung C, Chang Y. Design optimization of scroll compressor applied for frictional losses evaluation. *Int J Refrig*. 2010;**33**(3):615–624.

13 Etemad S, Nieter J. Design optimization of the scroll compressor. *Int J Refrig*. May 1989;**12**: 146–150.

14 Hirayama T, Ito Y, Shida S, Kawabe I, Hirano K. Development of large capacity rotary compressor with three cylinders. First report: prototype designs and their efficiencies. *Int J Refrig*. 2021;**130**: 278–287.

15 Meng X, Qi Y, Sheng L, Li Q, Su L. Investigations on efficiency improvement of rolling piston type rotary compressor with a new-designed cylinder. *Appl Therm Eng*. 2023;**222**: 119920.

16 Savvakis S, Dimopoulou G, Zoumpourlos K. The effect of the isolator design on the efficiency of rotary piston compressors. *Thermo*. 2023;**3**(2):216–231.

17 Noh K-Y, Min B-C, Song S-J, Yang J-S, Choi G-M, Kim D-J. Compressor efficiency with cylinder slenderness ratio of rotary compressor at various compression ratios. *Int J Refrig*. 2016;**70**: 42–56.

18 Gu H, Ye F, Chen Y, Wu J, Li W, Sundén B. Performance investigation and design optimization of novel rotating-cylinder sliding vane rotary compressors. *Int J Refrig*. 2022;**142**: 137–147.

19 Pelekis, Emmanouil Andreas, General Supply (Constructions) Co. Ltd. [Internet]; 1980 Aug 22 [cited 2022 Jul 25]. Available from: https://patentimages.storage.googleapis.com/52/03/a0/d6a3adfa53238a/EP0046586A2.pdf.

20 Duncan RJ. [Internet]; 2005 May 26 [cited 2022 Jul 25]. Available from: https://patentimages.storage.googleapis.com/27/7a/af/e922e7025ac297/US20050284440A1.pdf.

21 Lurtz JR. [Internet]; 2006 Jun 8 [cited 2022 Jul 25]. Available from: https://patentimages.storage.googleapis.com/27/98/25/0aff3dd7f209ff/US20060120910A1.pdf.

22 ASTRON AEROSPACE LLC. [Internet]; 2021 Feb 18 [cited 2022 Jul 25]. Available from: https://patentimages.storage.googleapis.com/05/ec/2f/3c5a66694e42df/WO2021029906A1.pdf.

23 BETA CAE Systems International AG. *ANSA 21.1.3 user's guide*, Switzerland; 2021.

24 Convergent Science. *Converge CFD 3.0 Manual*, Madison, Wisconsin; 2021.

25   Sullivan PE, Sehmby M. Internal force analysis of a variable displacement vane pump. In: *SAE World Congress and Exhibition*. Warrendale, PA: SAE; 2012.

26   Stosic N. On heat transfer in screw compressors. *Int J Heat Fluid Flow*. 2015;**51**: 285–297.

27   Roache PJ. Perspective: a method for uniform reporting of grid refinement studies. *J Fluids Eng*. 1994;**116**: 405–413.

28   Lin Y, Li X, Zhu Z, Wang X, Lin T, Cao H. An energy consumption improvement method for centrifugal pump based on bionic optimization of blade trailing edge. *Energy*. 2022;**246**: 123323.

29   Smith R, Inomata H, Peters C. *Supercritical fluid science and technology*. Amsterdam: Elsevier; 2013.